# Broadband electromagnetic characterization of a 100 Ω traveling-wave electrode by measuring scattering parameters

Fabrizio Consoli*
*Istituto Nazionale di Fisica Nucleare, Laboratori Nazionali del Sud, Via S. Sofia 62, 95125 Catania, Italy*

Pascal Balleyguier
*CEA/DAM/DIF, F-91297, Arpajon, France*

Marco Di Giacomo
*GANIL/SPIRAL2, Caen, France*

(Received 20 May 2012; revised manuscript received 28 April 2013; published 22 July 2013)

The Single Bunch Selector (SBS) will be used on the Spiral2 linear accelerator to reduce the rate of high energy bunches reaching the target with, in principle, no residual particles from the suppressed bunches. For this purpose, a pulsed electromagnetic wave will travel along the 100 Ω microstrip meander line electrode of the SBS. In this work we describe the broadband accurate characterization of the electrode electromagnetic features. The method applied here leads to the analytical determination of complex characteristic impedance, propagation constant, and group velocity from a measurement of the 50 Ω scattering parameters on the meander transmission line. Particular care is given to the de-embedding phase of the transitions required to connect the meander electrode to the measurement device.

DOI: 10.1103/PhysRevSTAB.16.072001 PACS numbers: 41.20.Jb, 84.37.+q, 84.40.−x, 41.85.Ct

## I. INTRODUCTION

The Spiral2 linear accelerator [1] is now under construction at GANIL Laboratories in Caen, France. The facility will supply accelerated particle beams at an operating frequency $f_{op} = 88.0525$ MHz. This value is too high for some time-of-flight experiments, and it is therefore important to have the possibility to reduce the rate of bunches reaching the experimental target, after they have been accelerated. In particular, it will be required to have only one bunch over $N$ (being $100 < N < 10000$) with, in principle, no residual particles from the suppressed bunches. These operations will be necessary already for the first experiments with the new Spiral2 beam, and will be performed by a *medium energy chopper*, called *Single Bunch Selector* [2–6]. In this traveling-wave device, a static magnetic steerer will permanently deviate the bunches on a dedicated *beam-stop* and a pulsed electromagnetic wave, traveling on a microstrip meander transmission line, will let the selected bunch be properly realigned and delivered to the downstream beam line [2,4]. A solution involving two parallel meander electrodes, fed by synchronized pulses with opposite amplitudes, was proposed in order to have good electric field transversal homogeneity and reduced power-handling problems. A compromise between the amount of radiofrequency power needed from the pulse supply, the amount of loss acceptable on the meander line (realized on alumina planar substrate) and the meander feasibility, has led to a value of 100 Ω for the characteristic impedance. This makes the rf characterization of the electrodes, and of the other related components, a challenging task. The first element of the rf chain circuit related to the single meander electrode is a 100 Ω − 1 kW power supply (DC coupled) suitable to produce the required pulse [4], that was supplied by the manufacturer with a custom 100 Ω coaxial output cable. The connection between this cable and the meander line electrode was one of the most delicate topics. Impedance matching, high voltage breakdown, cooling, and vacuum considerations have been taken into account for the design of a 100 Ω custom vacuum feedthrough, which has already been realized and characterized [4,6]. The feedthrough joins the cable to one side of the meander electrode; this connection is performed by means of a coaxial-microstrip transition [4]. Identical types of transitions are used to connect the other side of the meander line to the last element of the rf chain, a 100 Ω − 1 kW dummy load, by means of the usual custom 100 Ω coaxial cable supplied as load input [4].

The single pulse is required to travel along the slow-wave structure of the meander at the same velocity $v_b$ of the high energy particle bunch. In this case it is $\beta_b = v_b/c = 0.04$, with $c$ the velocity of light in vacuum. In order to reduce the residual particles of the suppressed

*Present address: Associazione Euratom-ENEA sulla Fusione, via E. Fermi 45, CP 65-00044 Frascati, Rome, Italy.
consoli@lns.infn.it

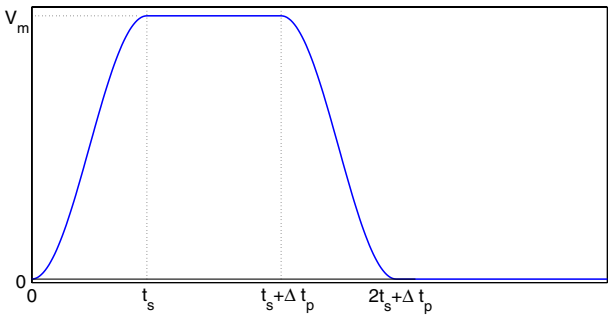


FIG. 1. Pulse model.

bunches and to maintain the beam emittance, it is important that the oscillations on the ground and on the high level of the propagating pulse are contained within 5% of the pulse maximum value. Thus, proper matching of the characteristic impedance of all the devices of the rf chain is required.

In this paper we describe a broadband and accurate method for the determination of complex characteristic impedance, propagation constant, and group velocity of this nonstandard 100 Ω microstrip meander line, from measurements of 50 Ω scattering parameters. The method is to be used in all parts of the rf chain of the single bunch selector, but it is applied here to the last version of the microstrip meander line [3,5]. It takes into account the influence due to the transitions connecting the meander line to the network analyzer, and it is applied for two different measurement setups of the electrode.

## II. MEASUREMENT DESCRIPTION

### A. Frequency range estimation

The single pulse $s(t)$ traveling on the electrode can be analytically modeled as described in Eq. (1) [4]:

$$s(t) = \begin{cases} \frac{V_m}{2}\left[1 - \cos\left(\pi \frac{t}{t_s}\right)\right] & 0 \le t \le t_s \\ V_m & t_s \le t \le t_A \\ \frac{V_m}{2}\left[1 + \cos\left(\pi \frac{t - t_A}{t_s}\right)\right] & t_A \le t \le t_B \end{cases} \quad (1)$$

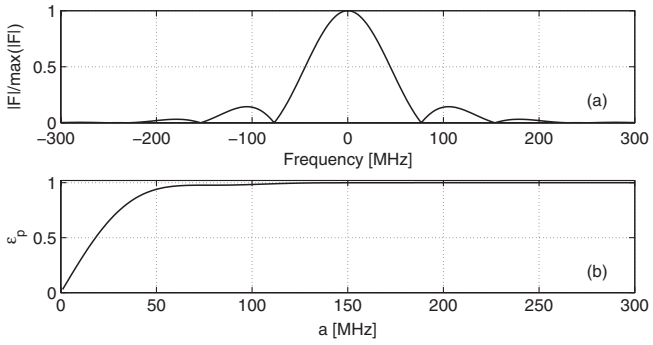


FIG. 2. (a) Normalized modulus of the pulse Fourier transform; (b) $\epsilon_p$ term versus frequency.

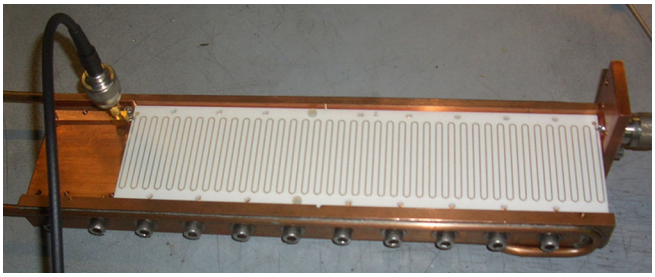

FIG. 3. Picture of the measurement setup for the meander line of the single bunch selector.

with $t_A = t_s + \Delta t_p$ and $t_B = 2t_s + \Delta t_p$. The pulse duration is FWHM $= t_A$. This is shown in Fig. 1.

The Fourier transform of this pulse is

$$F[s(t)](f) = V_m e^{-i\pi t_B f}[t_s F_1 + \Delta t_p \mathrm{sinc}(\Delta t_p f)], \quad (2)$$

where $\mathrm{sinc}(x) = \sin(\pi x)/(\pi x)$ and

$$F_1 = \cos(\pi f t_A) F_{11} - \tfrac{1}{2}\sin(\pi f t_A) F_{12}, \quad (3)$$

with

$$F_{11} = \mathrm{sinc}(t_s f), \quad (4a)$$

$$F_{12} = \mathrm{sinc}(t_s f + \tfrac{1}{2}) - \mathrm{sinc}(t_s f - \tfrac{1}{2}). \quad (4b)$$

In the present case it is $V_m = 2500$ V, $t_s = 6$ ns, $\Delta t_p = 7$ ns, FWHM $= 13$ ns. The *duty cycle* results $dc = \mathrm{FWHM} \cdot f_{\mathrm{op}}/N \rightarrow 1.14 \times 10^{-2}\% \le dc \le 1.14\%$. The related Fourier spectrum is shown in Fig. 2(a). We introduce the term

$$\epsilon_p = \frac{\int_{-a}^{+a} |F[s(t)](f)|^2 df}{E_P}, \quad (5)$$

where $E_P = \int_{-\infty}^{+\infty} |F[s(t)](f)|^2 df$ is the pulse overall energy. $\epsilon_p$ is the normalized pulse energy, resulting by integration over the $[-a, a]$ frequency interval. In Fig. 2(b) we represent the $\epsilon_p$ term versus the $a$ frequency. Figure 2 indicates that, for a suitable precision of the signal reconstruction, the pulse spectral content can be considered limited to 150 MHz. We choose to characterize the different parts of the single bunch selector for a frequency interval twice larger: 300 MHz.

### B. First measurement setup

We employed the measurement setup shown in Fig. 3. The last prototype of the microstrip electrode was manufactured on a 4.3 mm, 99.5% pure $Al_2O_3$ substrate. It is a plate with 39 meanders, with a total length of 273 mm [5]. It was placed on a copper housing, and connected with the HP 8753E Vector Network Analyzer by means of two 50 Ω transitions. The first (on the left of Fig. 3) is a 90° SMA connector joined to an SMA-N transition; the second is a jack $N$-type panel connector, on a thick copper flange. Then, both have different lengths. These types of 50 Ω

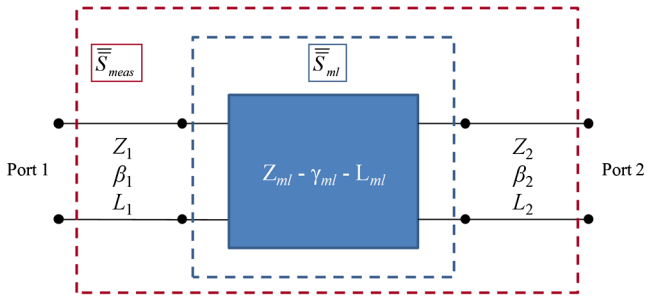


FIG. 4. Scheme of the measurement setup for the meander line.

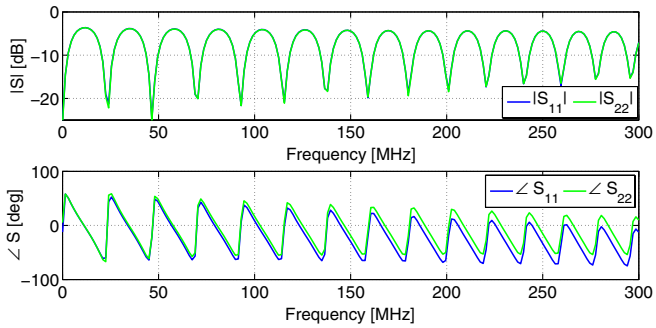


FIG. 6. Modulus and phase of $S_{11\,\mathrm{meas}}$ and $S_{22\,\mathrm{meas}}$.

transitions were chosen to provide a suitable connection of the network analyzer with the microstrip electrode placed on the conductive housing. A model of the apparatus is shown in Fig. 4.

The electrode that we want to characterize is indicated with the box at the center of the scheme. We consider it as a uniform transmission line, with characteristic impedance $Z_{\mathrm{ml}}$, propagation constant $\gamma_{\mathrm{ml}} = \alpha_{\mathrm{ml}} + i\beta_{\mathrm{ml}}$, and length $L_{\mathrm{ml}} = 273$ mm. After a proper calibration of the cables joining the vector network analyzer to the transitions, the "Port 1" of the analyzer is *connected directly* with the N-SMA transition. In Fig. 4 the calibration points of the network analyzer are those indicated with the labels *Port 1* and *Port 2*. They are connected with the central meander line by the two 50 Ω transitions, respectively. In this scheme, we model the SMA-N transition, the 90° SMA connector, and the junction between this and the meander line, as a 50 Ω uniform transmission line that we identify with the number "1." On the other side of the meander, we consider the complete block, connecting the electrode with the network analyzer, with the number "2." Then, it is $Z_1 = Z_2 = 50\ \Omega$ and

$$\beta_{12} \equiv \beta_1 = \beta_2 = \frac{\omega}{c} n_{12}, \tag{6}$$

where $n_{12}$ is the refraction index of the dielectric within the two coaxial junctions. If we consider this dielectric to be Teflon, we can set $n_{12} = \sqrt{2.1}$ over the whole frequency range. Their length is therefore the only difference between

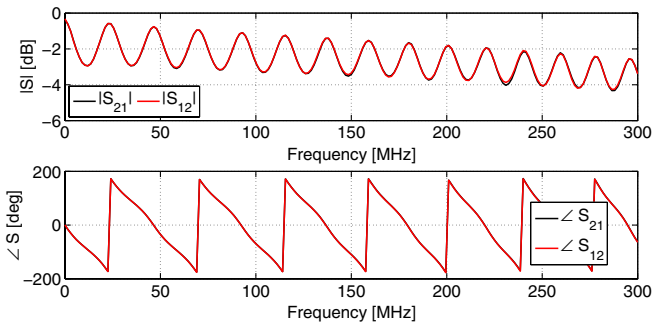


FIG. 5. Modulus and phase of $S_{21\,\mathrm{meas}}$ and $S_{12\,\mathrm{meas}}$.

the two transmission lines: $L_1 \neq L_2$. The $S$ parameters measured for this configuration by means of the network analyzer (indicated as tensor $\bar{\bar{S}}_{\mathrm{meas}}$ in Fig. 4), are shown in Figs. 5 and 6, for a typical 50 Ω normalization impedance.

We observe a difference between the $S_{11\,\mathrm{meas}}$ and $S_{22\,\mathrm{meas}}$ phases. Since the electrode that we are measuring is considered as an intrinsically symmetric structure, this is attributed to the different lengths $L_1$ and $L_2$. The accurate characterization of the meander line properties (described below) requires the determination of the $\bar{\bar{S}}_{\mathrm{ml}}$ tensor of Fig. 4 from the knowledge of $\bar{\bar{S}}_{\mathrm{meas}}$, by operating a proper de-embedding operation. This could be accomplished if suitable measured calibrations of the two transitions and relative joints to the meander line alone were supplied. However, this can be difficult in many situations, and particularly in this case. Alternatively, we use here a numerical method for the de-embedding procedure.

It is possible to show that [7]

$$\bar{\bar{S}}_{\mathrm{ml}} = \begin{bmatrix} S_{11\,\mathrm{ml}} & S_{12\,\mathrm{ml}} \\ S_{21\,\mathrm{ml}} & S_{22\,\mathrm{ml}} \end{bmatrix} = \begin{bmatrix} e^{i2\beta_{12}L_1} S_{11\,\mathrm{meas}} & e^{i\beta_{12}(L_1+L_2)} S_{12\,\mathrm{meas}} \\ e^{i\beta_{12}(L_1+L_2)} S_{21\,\mathrm{meas}} & e^{i2\beta_{12}L_2} S_{22\,\mathrm{meas}} \end{bmatrix}. \tag{7}$$

Because of the meander symmetry, we would expect to have $S_{11\,\mathrm{ml}} = S_{22\,\mathrm{ml}}$. From this condition, if we consider the generic term $S_{hk\,\mathrm{meas}} = |S_{hk\,\mathrm{meas}}| e^{i\varphi_{hk\,\mathrm{meas}}}$, it is possible to write

$$\Delta L_{12} = L_1 - L_2 = \frac{\varphi_{22\,\mathrm{meas}} - \varphi_{11\,\mathrm{meas}}}{2\beta_{12}} = \frac{c}{2n_{12}\omega}(\varphi_{22\,\mathrm{meas}} - \varphi_{11\,\mathrm{meas}}). \tag{8}$$

From Eq. (8) a simple numerical optimization was required, to overcome some uncertainties due to measurement errors, and the result was $\Delta L_{12} = 21.6$ mm. By using this value, it is possible to transform the measured matrix $\bar{\bar{S}}_{\mathrm{meas}}$ to an equivalent $\bar{\bar{S}}'_{\mathrm{meas}}$, relative to the model of an *effective configuration* where the two transmission lines have equal lengths ($L'_1 = L'_2 = L_2$):

$$\bar{\bar{S}}'_{\text{meas}} = \begin{bmatrix} S'_{11\,\text{meas}} & S'_{12\,\text{meas}} \\ S'_{21\,\text{meas}} & S'_{22\,\text{meas}} \end{bmatrix} = \begin{bmatrix} e^{i2\beta_{12}\Delta L_{12}} S_{11\,\text{meas}} & e^{i\beta_{12}\Delta L_{12}} S_{12\,\text{meas}} \\ e^{i\beta_{12}\Delta L_{12}} S_{21\,\text{meas}} & S_{22\,\text{meas}} \end{bmatrix}. \quad (9)$$

This transformation affects only the phases of the scattering parameters, which are shown in Fig. 7.

Thus, it is possible to get $\bar{\bar{S}}_{\text{ml}}$ matrix from $\bar{\bar{S}}'_{\text{meas}}$, by Eq. (10):

$$\bar{\bar{S}}_{\text{ml}} = \begin{bmatrix} e^{i2\beta_{12}L'_2} S'_{11\,\text{meas}} & e^{i2\beta_{12}L'_2} S'_{12\,\text{meas}} \\ e^{i2\beta_{12}L'_2} S'_{21\,\text{meas}} & e^{i2\beta_{12}L'_2} S'_{22\,\text{meas}} \end{bmatrix} = e^{i2\beta_{12}L'_2} \bar{\bar{S}}'_{\text{meas}}. \quad (10)$$

In order to estimate the remaining length $L'_2$, it is useful to determine the explicit expressions for the $\bar{\bar{S}}_{\text{ml}}$ parameters under the hypothesis of a uniform transmission line model. This is described in the Appendix. The results are

$$S_{11\,\text{ml}} = \frac{\tanh(\gamma_{\text{ml}}L_{\text{ml}})(\frac{Z_{\text{ml}}}{Z_{\text{in}}} - \frac{Z_{\text{in}}}{Z_{\text{ml}}})}{2 + \tanh(\gamma_{\text{ml}}L_{\text{ml}})(\frac{Z_{\text{ml}}}{Z_{\text{in}}} + \frac{Z_{\text{in}}}{Z_{\text{ml}}})}, \quad (11a)$$

$$S_{21\,\text{ml}} = \frac{\frac{4+4\tanh(\gamma_{\text{ml}}L_{\text{ml}})(\frac{Z_{\text{ml}}}{Z_{\text{in}}})}{2+\tanh(\gamma_{\text{ml}}L_{\text{ml}})(\frac{Z_{\text{ml}}}{Z_{\text{in}}}+\frac{Z_{\text{in}}}{Z_{\text{ml}}})}}{(1 + \frac{Z_{\text{ml}}}{Z_{\text{in}}})e^{\gamma_{\text{ml}}L_{\text{ml}}} + (1 - \frac{Z_{\text{ml}}}{Z_{\text{in}}})e^{-\gamma_{\text{ml}}L_{\text{ml}}}}, \quad (11b)$$

where the generic normalization impedance $Z_{\text{in}}$ has been used. From Eq. (11) it is possible to write (see the Appendix)

$$S_{11\,\text{ml}} = \frac{\tanh(\gamma_{\text{ml}}L_{\text{ml}})(X^2 - 1)}{2X + \tanh(\gamma_{\text{ml}}L_{\text{ml}})(X^2 + 1)}, \quad (12a)$$

$$S^2_{21\,\text{ml}} = \frac{4X^2[1 - \tanh^2(\gamma_{\text{ml}}L_{\text{ml}})]}{[2X + \tanh(\gamma_{\text{ml}}L_{\text{ml}})(X^2 + 1)]^2}, \quad (12b)$$

where $X = Z_{\text{ml}}/Z_{\text{in}}$. The meander symmetry gives

$$S_{11\,\text{ml}} = S_{22\,\text{ml}} \qquad S_{21\,\text{ml}} = S_{12\,\text{ml}}. \quad (13)$$

It is then possible to solve the system from the simplified expressions (12), and obtain

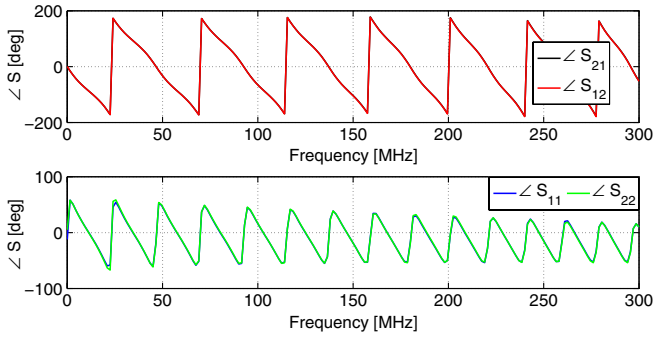


FIG. 7. Phases of the $S'_{\text{meas}}$ parameters.

$$\tanh^2(\gamma_{\text{ml}}L_{\text{ml}}) = [(1 + S_{11\,\text{ml}})^2 - S^2_{21\,\text{ml}}][(1 - S_{11\,\text{ml}})^2 - S^2_{21\,\text{ml}}] \times [1 - S^2_{11\,\text{ml}} + S^2_{21\,\text{ml}}]^{-2} \quad (14)$$

and

$$X^2 = \frac{(1 + S_{11\,\text{ml}})^2 - S^2_{21\,\text{ml}}}{(1 - S_{11\,\text{ml}})^2 - S^2_{21\,\text{ml}}}. \quad (15)$$

Equation (15) was also achieved in Refs. [8,9], where a method employing even and odd mode excitations of the network, different from that described in the Appendix, was used.

In order to achieve conditions for the numerical estimation of the length $L'_2$, we write

$$|\tanh(\gamma_{\text{ml}}L_{\text{ml}})|^2 = \frac{\tanh^2(\alpha_{\text{ml}}L_{\text{ml}}) + \tan^2(\beta_{\text{ml}}L_{\text{ml}})}{1 + \tanh^2(\alpha_{\text{ml}}L_{\text{ml}})\tan^2(\beta_{\text{ml}}L_{\text{ml}})}. \quad (16)$$

Since for these meander structures it is generally true that $0 < \alpha_{\text{ml}}L_{\text{ml}} < 1$ (see also Fig. 11), this function will have

$$\min[|\tanh(\gamma_{\text{ml}}L_{\text{ml}})|^2] = \tanh^2(\alpha_{\text{ml}}L_{\text{ml}}) \quad (17)$$

for $\beta_{\text{ml}}L_{\text{ml}} = k\pi$ and

$$\max[|\tanh(\gamma_{\text{ml}}L_{\text{ml}})|^2] = \tanh^{-2}(\alpha_{\text{ml}}L_{\text{ml}}) \quad (18)$$

for $\beta_{\text{ml}}L_{\text{ml}} = \pi(2k + 1)/2$, with $k \in \mathbb{Z}$. In addition, it must be

$$\angle[\tanh(\gamma_{\text{ml}}L_{\text{ml}})] = 0 \quad (19)$$

for $\beta_{\text{ml}}L_{\text{ml}} \in \{k\pi; \pi(2k + 1)/2\}$. Figures 5 and 6 show that the modulus of the $S_{hk\,\text{meas}}$ parameters presents many local minima and maxima with respect to frequency. From Eq. (7) it is also true that $|S_{hk\,\text{ml}}| = |S_{hk\,\text{meas}}|$. From Eqs. (12a) and (12b) it is possible to show that these local minima and maxima are achieved for frequencies very close to those $\{\omega_a\}$ where the condition (19) is fulfilled. Then, it is possible to determine the length $L'_2$ numerically, in order to make the conditions (17)–(19) true for these frequencies $\{\omega_a\}$. In particular, the condition achieved for $\beta_{\text{ml}}L_{\text{ml}} = \pi(2k + 1)/2$ is related to the maxima of $|S_{11\,\text{meas}}|$, and as a result the measurement errors are minimized in this case. For better accuracy, we have always considered this condition. The result is $L'_2 = 8.2$ mm. Of course, the numerical process is improved when many frequency points are supplied for the measured $S_{hk\,\text{meas}}$. The phases of the $S_{\text{ml}}$ parameters, obtained in this way, are given in Fig. 8.

We can now determine the meander characteristics at the frequencies where $\beta_{\text{ml}}L_{\text{ml}} = \pi(2k + 1)/2$. $Z_{\text{ml}}$, achieved from Eq. (15), is shown in Figs. 9 and 10. $\gamma_{\text{ml}}L_{\text{ml}}$ is achieved from Eq. (14). The real part $\alpha_{\text{ml}}L_{\text{ml}}$ is plotted in Fig. 11. From the knowledge of the $\beta_{\text{ml}}$ term it is possible to derive the propagation group velocity of the pulsed electromagnetic wave on the meander line

$$v_g = \frac{d\omega}{d\beta_{\text{ml}}}, \quad (20)$$

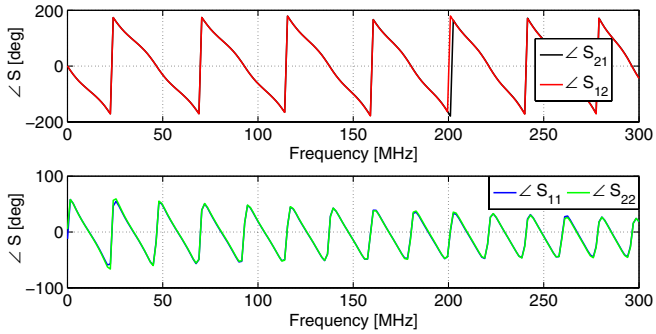


FIG. 8. Phases of the $S_{\mathrm{ml}}$ parameters.

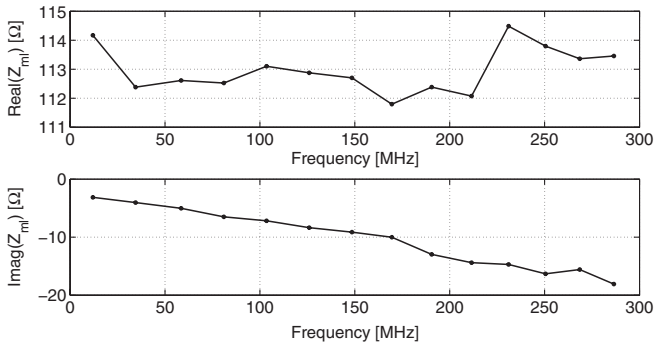


FIG. 9. Real and imaginary part of $Z_{\mathrm{ml}}$ for the frequencies where $\beta_{\mathrm{ml}}L_{\mathrm{ml}} = \pi(2k+1)/2$.

which is shown in Fig. 11. The determination of $v_g$ required a numerical fit to the $\beta_{\mathrm{ml}}$ function, necessary to produce a suitable derivative operation.

From the $\bar{\bar{S}}_{\mathrm{ml}}$ parameters, obtained with a typical $Z_0$ normalization impedance of 50 Ω, it is possible to achieve the $\bar{\bar{S}}_{\mathrm{ml\,100}}$ parameters relative to $Z_0 = 100$ Ω, by applying the formula [7]

$$\bar{\bar{S}}_{\mathrm{ml\,100}} = [50(\bar{\bar{I}} + \bar{\bar{S}}_{\mathrm{ml\,50}})(\bar{\bar{I}} - \bar{\bar{S}}_{\mathrm{ml\,50}})^{-1} - 100\bar{\bar{I}}] \times [50(\bar{\bar{I}} + \bar{\bar{S}}_{\mathrm{ml\,50}})(\bar{\bar{I}} - \bar{\bar{S}}_{\mathrm{ml\,50}})^{-1} + 100\bar{\bar{I}}]^{-1}, \quad (21)$$

where $\bar{\bar{I}}$ is the identity matrix. This transformation is very useful for the future characterization of the complete rf chain. The resulting $\bar{\bar{S}}_{\mathrm{ml\,100}}$ parameters are given in Figs. 12 and 13.

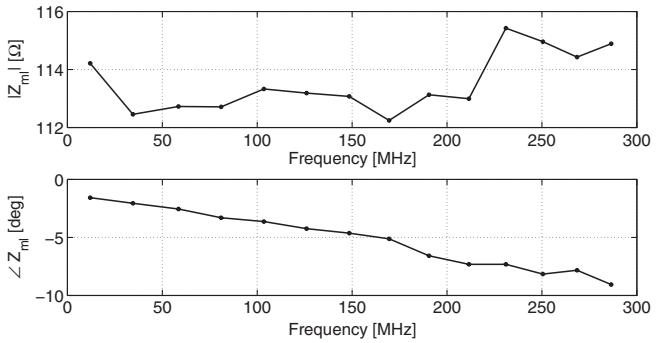


FIG. 10. Modulus and phase of $Z_{\mathrm{ml}}$ for the frequencies where $\beta_{\mathrm{ml}}L_{\mathrm{ml}} = \pi(2k+1)/2$.

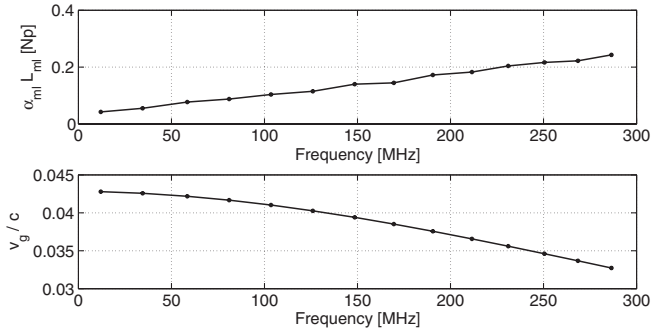


FIG. 11. $\alpha_{\mathrm{ml}}L_{\mathrm{ml}}$ and $v_g/c$ for the frequencies where $\beta_{\mathrm{ml}}L_{\mathrm{ml}} = \pi(2k+1)/2$; $c$ is the light velocity in vacuum.

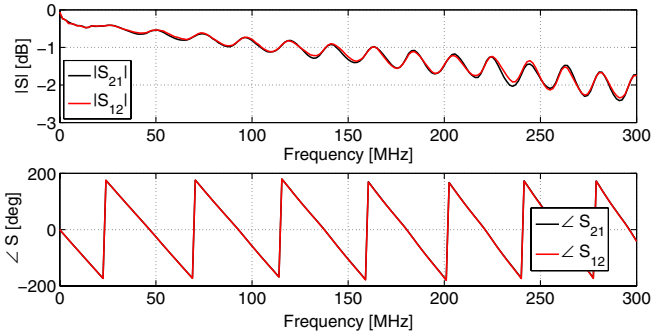


FIG. 12. Modulus and phase of $S_{21\,\mathrm{ml}}$ and $S_{12\,\mathrm{ml}}$, normalized to 100 Ω impedance.

### C. Second measurement setup

In this measurement setup a different type of solution was found to connect Port 1 to the meander, as described in Ref. [4] (see Fig. 14). The copper housing, having 17 mm thickness, was drilled under the alumina plate. The diameter of the hole was 16 mm on the first 2.5 mm, and 6 mm on the remaining depth (i.e. 14.5 mm), closer to the alumina plate. A flat panel $N$-type connector was used, and the central conductor was joined to a circular pad on the meander line, through a hole on the alumina substrate.

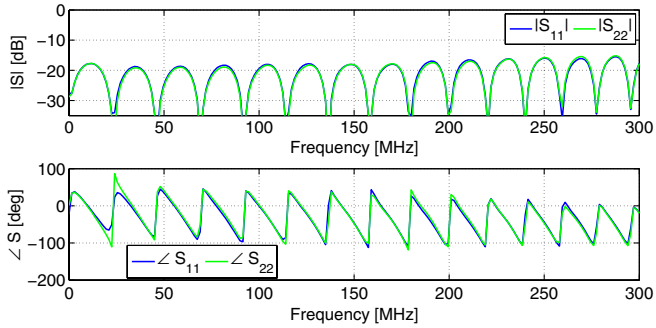


FIG. 13. Modulus and phase of $S_{11\,\mathrm{ml}}$ and $S_{22\,\mathrm{ml}}$, normalized to 100 Ω impedance.

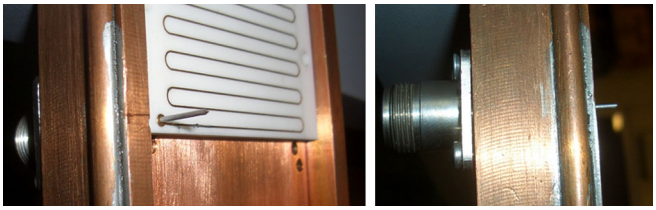

FIG. 14. Pictures of the measurement setup for the meander line of the single bunch selector. Change in the coaxial transition of Port 1.

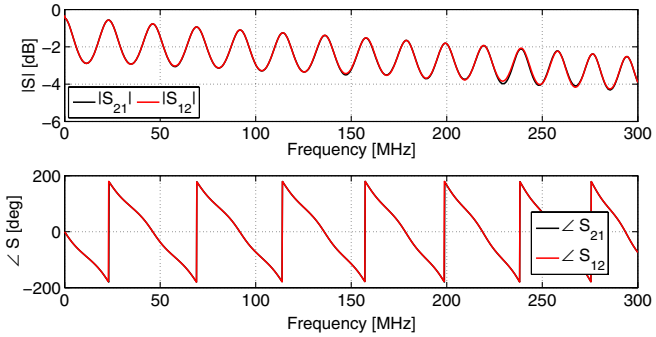


FIG. 15. Modulus and phase of $S_{21\,\mathrm{meas}}$ and $S_{12\,\mathrm{meas}}$.

The measured scattering parameters $\bar{\bar{S}}_{\mathrm{meas}}$ of this case are shown in Figs. 15 and 16, with a typical normalization impedance of 50 Ω. By taking into account the new transition for Port 1 and applying the procedure described in the previous section for de-embedding, we found a new final matrix $\bar{\bar{S}}_{\mathrm{ml}}$, whose elements have phases shown in Fig. 17. The next diagrams summarize and compare the results obtained with the two different measurement setups for the same meander line. The impedance $Z_{\mathrm{ml}}$ is represented in Figs. 18 and 19, while the product $\alpha_{\mathrm{ml}}L_{\mathrm{ml}}$ and $v_g$ are in Fig. 20.

### D. Considerations on the proposed method

The two different measurements of each parameter appear to be in good agreement, and only small differences are present on the $Z_{\mathrm{ml}}$ modulus and phase at higher frequencies. In particular, the phase difference is contained

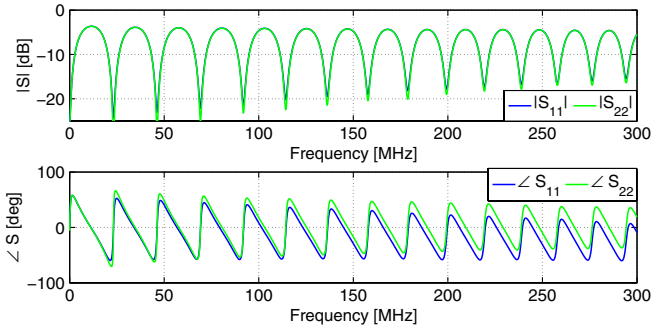


FIG. 16. Modulus and phase of $S_{11\,\mathrm{meas}}$ and $S_{22\,\mathrm{meas}}$.

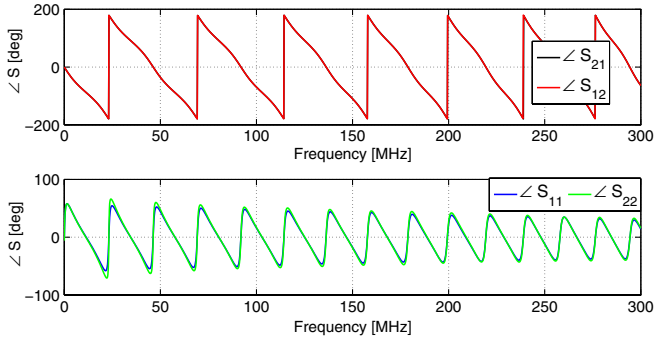


FIG. 17. Phases of the $S_{\mathrm{ml}}$ parameters.

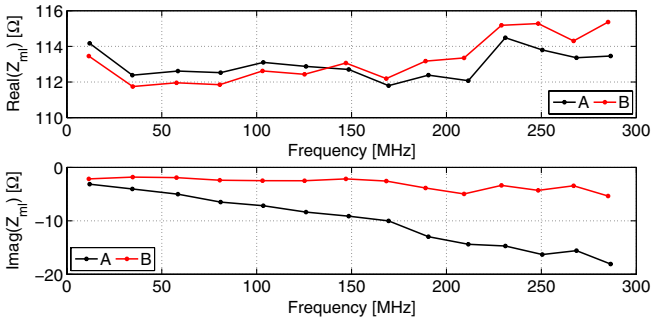


FIG. 18. Real and imaginary part of $Z_{\mathrm{ml}}$ for the frequencies where $\beta_{\mathrm{ml}}L_{\mathrm{ml}} = \pi(2k+1)/2$. Comparison between the measurements performed with the two different setups: (A) first setup; (B) second setup.

within the range of 4 degrees up to 150 MHz. These differences can be due to the two main assumptions used in the layout modeling. The first is about the possibility to consider the meander line as a symmetric structure: a transmission line with uniform characteristic impedance and propagation constant. The not perfect planarity of the copper housing could slightly affect this hypothesis. The second is with regards to the modeling of the two transitions, from the meander line to the network analyzer, as uniform 50 Ω transmission lines, without taking into

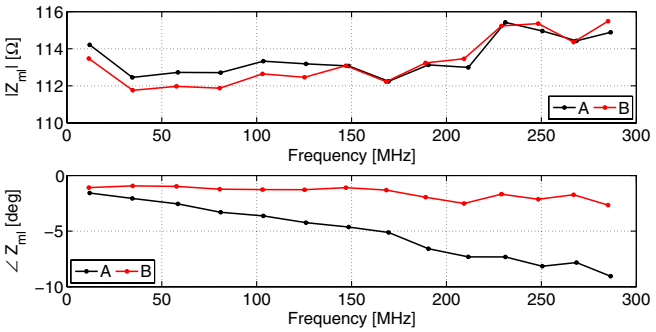


FIG. 19. Modulus and phase of $Z_{\mathrm{ml}}$ for the frequencies where $\beta_{\mathrm{ml}}L_{\mathrm{ml}} = \pi(2k+1)/2$. Comparison between the measurements performed with the two different setups: (A) first setup; (B) second setup.

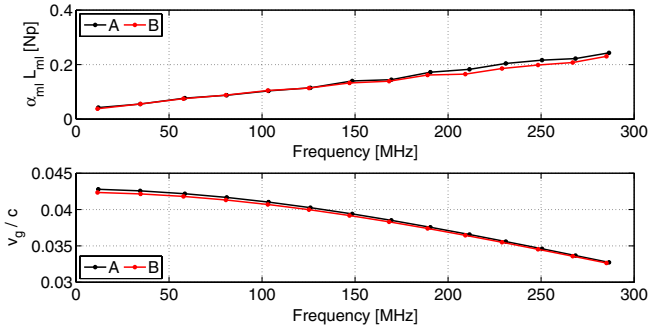


FIG. 20. $\alpha_{\mathrm{ml}} L_{\mathrm{ml}}$ and $v_g/c$ for the frequencies where $\beta_{\mathrm{ml}} L_{\mathrm{ml}} = \pi(2k+1)/2$; $c$ is the light velocity in vacuum. Comparison between the measurements performed with the two different setups: (A) first setup; (B) second setup.

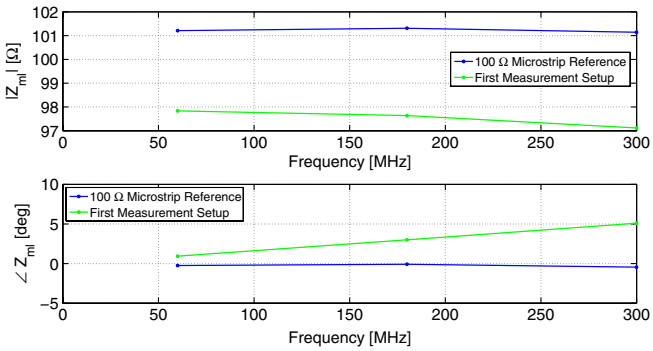


FIG. 21. Electromagnetic simulations of the 100 Ω straight microstrip line, 500 mm long: modulus and phase of the $Z_{\mathrm{ml}}$ for the frequencies where $\beta_{\mathrm{ml}} L_{\mathrm{ml}} = \pi(2k+1)/2$; comparison between the simulated reference, and the case with the coaxial-microstrip transitions of the *first measurements setup*, shown in Fig. 3.

account the local changes in their characteristic impedances, in particular due to the coaxial-microstrip junctions.

Application, to the present case, of classical frequency-domain techniques, commonly used for calibration and de-embedding when performing rf and microwave measurements (like *SOLT*, *TRL*, *LRL*, *LRM*, ... [10–13]), would require calibration references (*Open*, *Short*, *Thru*, *Line*, ...) made on the same alumina substrate, with microstrips realized at the same time and using the same process producing the meander line electrode. Thus, these techniques could be also suitable to verify the characterization of future electrodes, provided those references will be simultaneously reproduced, but at the price of a remarkable increase on the electrode production costs. The method developed and discussed in the present work was indeed necessary because of the lack of those standard references for the realized electrode.

*Time-domain reflectometry* (TDR) measurements [10,14–16] could in principle supply some verification of the method we propose, in particular for the de-embedding. Anyway, in this case the required measurement spatial resolution of around 1 mm is a very difficult issue, because it imposes very short rise and fall times for the propagating probe pulse. This would imply a very large frequency content, of many tens of GHz [10,14–16]. Thus, an accurate measurement requires that the meander line-coaxial transitions have a suitable behavior, in terms of intrinsic impedance and low radiation properties, for such a very broad frequency range. This is the main limiting factor for the application of this method to these types of measurements. Another issue is the necessity to use very expensive apparatuses and calibration kits with such wide bandwidths, although the measurements are really needed only up to 150–300 MHz.

In order to further estimate the accuracy of the proposed method, we performed some full-wave electromagnetic simulations by CST MICROWAVE STUDIO solver. We considered just a nominal 100 Ω straight microstrip, 500 mm long, on the same 4.3 mm thick alumina-type substrate of the meander line. We numerically determined the $\bar{\bar{S}}$ parameters, and then the $Z_{\mathrm{ml}}$ by applying Eq. (15). Results are given in Fig. 21 for the frequencies where $\beta_{\mathrm{ml}} L_{\mathrm{ml}} = \pi(2k+1)/2$. We did not consider the term $\alpha_{\mathrm{ml}} L_{\mathrm{ml}}$, because in this case the structure has intrinsically low loss. In a second step, within the simulations we further included the two coaxial-microstrip transitions, accurately modeled from those (SMA microstrip the first, and N-microstrip the second) used in the *first measurements setup*, shown in Fig. 3. We used in this case the described de-embedding procedure, and then $Z_{\mathrm{ml}}$ was determined by Eq. (15), as graphically represented in Fig. 21.

We see that there is good agreement with the reference. The small differences can be due to the numerical procedure, and also to the assumption of the two coaxial-microstrip transitions to be ideal 50 Ω lines. The simulations also indicated that the main differences are produced from the second transition (*N*-type microstrip on the thick copper flange), while the first (SMA-type microstrip) appears to better follow the 50 Ω characteristic impedance. In the *second measurement setup* the SMA-microstrip transition was changed, with the structure shown in Fig. 14, while maintaining the first transition (N microstrip). The very good agreement obtained by the two measurement results in Figs. 18–20 appears to be an indication of the good performances of both the SMA-microstrip transition and the one of Fig. 14, and of the accuracy of the proposed method.

## III. CONCLUSION

The two measurements reveal that there is more than a 10% difference on the electrode characteristic impedance, with respect to the ideal 100 Ω project requirement, up to 150 MHz. Attenuation due to the line is small, but non-negligible. The normalized group velocity results are a little higher than the bunch velocity corresponding to

$\beta_b = 0.04$. An improved insight on the electrode realization, and on its mechanical and electrical matching on the dedicated copper housing, is therefore required.

The method described here provides improved and broader results with respect to those described in Ref. [5]. The real and imaginary parts of $Z_{\rm ml}$ and $\gamma_{\rm ml}$, and the $\alpha_{\rm ml}L_{\rm ml}$ meander attenuation term, are estimated over a wide band, as well as the pulse propagation velocity. As the effects of the transitions from the meander line to the network analyzer are taken into account, the determination of the line parameters is more accurate [9]. This method will be useful for future measurements on the other elements of the complete prototype of the single bunch selector, as well as on the meander electrodes on the final housing, where the second transversal type of described transition will be used. In addition, it can be applied to characterize passive structures similar to the type here described, and in more general situations where the classical frequency-domain (*SOLT*, *TRL*, *LRL*, *LRM*, ...) and time-domain (TDR) techniques are not applicable.

## ACKNOWLEDGMENTS

The authors would like to thank A. Caruso, from Istituto Nazionale di Fisica Nucleare–Laboratori Nazionali del Sud, for his help in performing the measurements and G. F. Grinyer from GANIL/SPIRAL2 for carefully reading the manuscript.

## APPENDIX

We here describe the derivation of Eq. (11) relative to the network of Fig. 4. We consider the scheme represented in Fig. 22, where a generic network with characteristic impedance $Z_{\rm ml}$, propagation constant $\gamma_{\rm ml}$, and length $L_{\rm ml}$ is connected to a load (at Port 2), by means of a network with propagation constant $\gamma_L$ and characteristic impedance $Z_L$, supposed equal to the load impedance. In the same way, the generator (at the input Port 1) is connected to the network ml by means of a line with propagation constant $\gamma_{\rm in}$ and characteristic impedance $Z_{\rm in}$, supposed equal to the generator impedance $Z_G$. These assumptions are made to avoid the consideration of multiple reflections at the load and at the generator sides, and were commonly fulfilled in the measurement setups that we used to determine the scattering parameters.

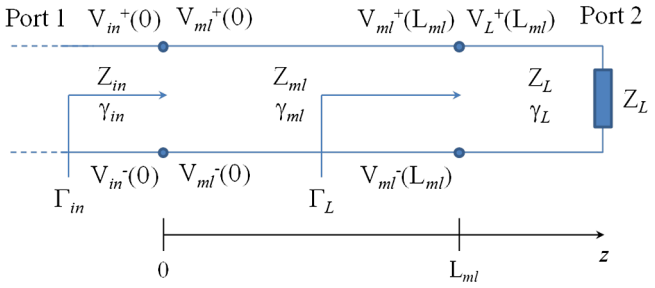


FIG. 22. Scheme for the determination of $\bar{\bar{S}}_{\rm ml}$.

From transmission line theory [7], the voltage across the network ml can be written as

$$V_{\rm ml}(z) = V^+_{\rm ml0}e^{-\gamma_{\rm ml}z} + V^-_{\rm ml0}e^{+\gamma_{\rm ml}z} \tag{A1}$$

for $0 \le z \le L_{\rm ml}$. From Fig. 22, it is $V^+_{\rm ml}(z) = V^+_{\rm ml0}e^{-\gamma_{\rm ml}z}$ and $V^-_{\rm ml}(z) = V^-_{\rm ml0}e^{+\gamma_{\rm ml}z}$. In a similar way, the voltage relative to the waves from the generator side (input) can be written as

$$V_{\rm in}(z) = V^+_{\rm in0}e^{-\gamma_{\rm in}z} + V^-_{\rm in0}e^{+\gamma_{\rm in}z} \tag{A2}$$

for $z \le 0$, where $V^+_{\rm in}(z) = V^+_{\rm in0}e^{-\gamma_{\rm in}z}$ and $V^-_{\rm in}(z) = V^-_{\rm in0}e^{+\gamma_{\rm in}z}$. The load is matched to its network, and therefore no reflection will occur. Then, it is

$$V_L(z) = V^+_L(z) = V^+_{L0}e^{-\gamma_L z} \tag{A3}$$

for $z \ge L_{\rm ml}$. The reflection coefficient at the transition between the generator network and the network ml (i.e. for $z = 0$) is defined as

$$\Gamma_{\rm in} = \frac{V^-_{\rm in}(0)}{V^+_{\rm in}(0)} = S_{11\,\rm ml} \tag{A4}$$

and it is equal to the scattering term $S_{11\,\rm ml}$, for definition, relative to Port 1. This can be calculated as [7]

$$\Gamma_{\rm in} = \frac{Z_1 - Z_{\rm in}}{Z_1 + Z_{\rm in}}, \tag{A5}$$

where

$$Z_1 = Z_{\rm ml}\frac{Z_L + Z_{\rm ml}\tanh(\gamma_{\rm ml}L_{\rm ml})}{Z_{\rm ml} + Z_L\tanh(\gamma_{\rm ml}L_{\rm ml})} \tag{A6}$$

is the impedance $Z_L$ transformed by the network ml. By combining Eqs. (A4)–(A6), it is possible to achieve

$$\begin{aligned} S_{11\,\rm ml} = {} & [(Z^2_{\rm ml} - Z_L Z_{\rm in})\tanh(\gamma_{\rm ml}L_{\rm ml}) + Z_{\rm ml}(Z_L - Z_{\rm in})] \\ & \times [(Z^2_{\rm ml} + Z_L Z_{\rm in})\tanh(\gamma_{\rm ml}L_{\rm ml}) + Z_{\rm ml}(Z_L + Z_{\rm in})]^{-1}. \end{aligned} \tag{A7}$$

If $Z_L = Z_{\rm in}$, classical case when a network analyzer is used for measuring the transmission line, we achieve

$$S_{11\,\rm ml} = \frac{\tanh(\gamma_{\rm ml}L_{\rm ml})(\frac{Z_{\rm ml}}{Z_{\rm in}} - \frac{Z_{\rm in}}{Z_{\rm ml}})}{2 + \tanh(\gamma_{\rm ml}L_{\rm ml})(\frac{Z_{\rm ml}}{Z_{\rm in}} + \frac{Z_{\rm in}}{Z_{\rm ml}})}, \tag{A8}$$

which is Eq. (11a). We now want to determine the term $S_{21\,\rm ml}$ explicitly. First, we write Eq. (A2) as

$$V_{\rm in}(z) = V^+_{\rm in0}(e^{-\gamma_{\rm in}z} + \Gamma_{\rm in}e^{+\gamma_{\rm in}z}) \tag{A9}$$

by making use of Eq. (A4). In the same way, it is possible to write Eq. (A1) as

$$V_{\mathrm{ml}}(z) = V^{+}_{\mathrm{ml}0} e^{-\gamma_{\mathrm{ml}} L_{\mathrm{ml}}} \left[ e^{-\gamma_{\mathrm{ml}}(z-L_{\mathrm{ml}})} + \frac{V^{-}_{\mathrm{ml}0} e^{+\gamma_{\mathrm{ml}} L_{\mathrm{ml}}}}{V^{+}_{\mathrm{ml}0} e^{-\gamma_{\mathrm{ml}} L_{\mathrm{ml}}}} e^{\gamma_{\mathrm{ml}}(z-L_{\mathrm{ml}})} \right]$$
$$= V^{+}_{\mathrm{ml}0} e^{-\gamma_{\mathrm{ml}} L_{\mathrm{ml}}} [e^{-\gamma_{\mathrm{ml}}(z-L_{\mathrm{ml}})} + \Gamma_L e^{\gamma_{\mathrm{ml}}(z-L_{\mathrm{ml}})}], \quad \text{(A10)}$$

where

$$\Gamma_L = \frac{V^{-}_{\mathrm{ml}0} e^{+\gamma_{\mathrm{ml}} L_{\mathrm{ml}}}}{V^{+}_{\mathrm{ml}0} e^{-\gamma_{\mathrm{ml}} L_{\mathrm{ml}}}} = \frac{Z_L - Z_{\mathrm{ml}}}{Z_L + Z_{\mathrm{ml}}} \quad \text{(A11)}$$

is the reflection coefficient at the load side ($z = L_{\mathrm{ml}}$). At the transition between the network ml and the generator network ($z = 0$), it is $V_{\mathrm{ml}}(0) = V_{\mathrm{in}}(0)$ that gives

$$V^{+}_{\mathrm{ml}0} e^{-\gamma_{\mathrm{ml}} L_{\mathrm{ml}}} (e^{\gamma_{\mathrm{ml}} L_{\mathrm{ml}}} + \Gamma_L e^{-\gamma_{\mathrm{ml}} L_{\mathrm{ml}}}) = V^{+}_{\mathrm{in}0}(1 + \Gamma_{\mathrm{in}}), \quad \text{(A12)}$$

by combining Eqs. (A9) and (A10). In the same way, at the transition between the network ml and the load network ($z = L_{\mathrm{ml}}$), it is $V_{\mathrm{ml}}(L_{\mathrm{ml}}) = V_L(L_{\mathrm{ml}})$:

$$V^{+}_{\mathrm{ml}0} e^{-\gamma_{\mathrm{ml}} L_{\mathrm{ml}}} (1 + \Gamma_L) = V^{+}_{L0} e^{-\gamma_L L_{\mathrm{ml}}}, \quad \text{(A13)}$$

by combining Eqs. (A3) and (A10). By definition, it is

$$S_{21\,\mathrm{ml}} = \frac{V^{+}_{L0} e^{-\gamma_L L_{\mathrm{ml}}}}{V^{+}_{\mathrm{in}0}} = \frac{(1 + \Gamma_L)(1 + \Gamma_{\mathrm{in}})}{e^{\gamma_{\mathrm{ml}} L_{\mathrm{ml}}} + \Gamma_L e^{-\gamma_{\mathrm{ml}} L_{\mathrm{ml}}}}, \quad \text{(A14)}$$

where Eqs. (A12) and (A13) have been used. If $Z_L = Z_{\mathrm{in}}$ we achieve

$$S_{21\,\mathrm{ml}} = \frac{\frac{4 + 4\tanh(\gamma_{\mathrm{ml}} L_{\mathrm{ml}}) \left(\frac{Z_{\mathrm{ml}}}{Z_{\mathrm{in}}}\right)}{2 + \tanh(\gamma_{\mathrm{ml}} L_{\mathrm{ml}}) \left(\frac{Z_{\mathrm{ml}}}{Z_{\mathrm{in}}} + \frac{Z_{\mathrm{in}}}{Z_{\mathrm{ml}}}\right)}}{\left(1 + \frac{Z_{\mathrm{ml}}}{Z_{\mathrm{in}}}\right) e^{\gamma_{\mathrm{ml}} L_{\mathrm{ml}}} + \left(1 - \frac{Z_{\mathrm{ml}}}{Z_{\mathrm{in}}}\right) e^{-\gamma_{\mathrm{ml}} L_{\mathrm{ml}}}}, \quad \text{(A15)}$$

where (A5) and (A11) have been used. This is Eq. (11b). If we consider $X = Z_{\mathrm{ml}}/Z_{\mathrm{in}}$, we can write

$$S_{11\,\mathrm{ml}} = \frac{\tanh(\gamma_{\mathrm{ml}} L_{\mathrm{ml}})(X^2 - 1)}{2X + \tanh(\gamma_{\mathrm{ml}} L_{\mathrm{ml}})(X^2 + 1)}, \quad \text{(A16a)}$$

$$S_{21\,\mathrm{ml}} = \frac{\frac{4X[1 + X\tanh(\gamma_{\mathrm{ml}} L_{\mathrm{ml}})]}{2X + \tanh(\gamma_{\mathrm{ml}} L_{\mathrm{ml}})(X^2+1)}}{(1 + X) e^{\gamma_{\mathrm{ml}} L_{\mathrm{ml}}} + (1 - X) e^{-\gamma_{\mathrm{ml}} L_{\mathrm{ml}}}}. \quad \text{(A16b)}$$

It is possible to write

$$[(1 + X) e^{\gamma_{\mathrm{ml}} L_{\mathrm{ml}}} + (1 - X) e^{-\gamma_{\mathrm{ml}} L_{\mathrm{ml}}}]^{-1}$$
$$= \pm \frac{\sqrt{1 - \tanh^2(\gamma_{\mathrm{ml}} L_{\mathrm{ml}})}}{2[1 + X\tanh(\gamma_{\mathrm{ml}} L_{\mathrm{ml}})]}, \quad \text{(A17)}$$

where the choice for the $\pm$ depends on the product $\gamma_{\mathrm{ml}} L_{\mathrm{ml}}$. When we substitute this result into Eq. (A16b) we get

$$S_{11\,\mathrm{ml}} = \frac{\tanh(\gamma_{\mathrm{ml}} L_{\mathrm{ml}})(X^2 - 1)}{2X + \tanh(\gamma_{\mathrm{ml}} L_{\mathrm{ml}})(X^2 + 1)}, \quad \text{(A18a)}$$

$$S^2_{21\,\mathrm{ml}} = \frac{4X^2[1 - \tanh^2(\gamma_{\mathrm{ml}} L_{\mathrm{ml}})]}{[2X + \tanh(\gamma_{\mathrm{ml}} L_{\mathrm{ml}})(X^2 + 1)]^2} \quad \text{(A18b)}$$

which is the final expression of Eq. (12).


[1] M. Di Giacomo, in *Proceedings of the 12th International Workshop on RF Superconductivity* (Cornell University, Ithaca, New York, 2005), pp. 632–636 [http://www.jacow.org].

[2] G. Le Dem and M. Di Giacomo, in *Proceedings of the 2007 Particle Accelerator Conference, Albuquerque, New Mexico* (IEEE, New York, 2007), pp. 158–160, [http://www.jacow.org].

[3] P. Balleyguier, M. Di Giacomo, M. Michel, G. Freemont, and P. Bertrand, in *Proceedings of the 25th International Linear Accelerator Conference LINAC10, Tsukuba, Japan* (KEK, Tsukuba, Japan, 2010), pp. 286–288 [http://www.jacow.org].

[4] F. Consoli, A. Caruso, G. Gallo, D. Rifuggiato, E. Zappala', and M. Di Giacomo, in *Proceedings of the 2011 Particle Accelerator Conference, NY, USA* (IEEE, New York, 2011), pp. 1346–1348 [http://www.jacow.org].

[5] M. Di Giacomo, P. Balleyguier, F. Consoli, A. Caruso, and A. Longhitano, in *Proceedings of the 2nd International Particle Accelerator Conference, San Sebastián, Spain* (EPS-AG, Spain, 2011), pp. 1710–1712 [http://www.jacow.org].

[6] M. Di Giacomo, A. Caruso, G. Gallo, E. Zappala', D. Rifuggiato, A. Longhitano, and F. Consoli, in *Proceedings of the 3rd International Particle Accelerator Conference, New Orleans, Louisiana, USA, 2012* (IEEE, Piscataway, NJ, 2012), pp. 2663–2665 [http://www.jacow.org].

[7] D. M. Pozar, *Microwave Engineering* (Wiley, New York, 2004), 3rd ed.

[8] Yi-Chi Shih, Microwave J., pages 95–105 (April 1991).

[9] D. F. Williams and R. B. Marks, IEEE Microwave Guided Wave Lett. **3**, 247 (1993).

[10] S. Reyes, Microwave J., pages 64–83 (March 2005).

[11] S. Amakawa, N. Ishihara, and K. Masu, in Advanced Microwave Circuits and Systems, edited by V. Zhurbenko (InTech, 2010), Chap. 2, pp. 13–32 [http://www.intechopen.com/books/advanced-microwave-circuits-and-systems].

[12] T. Hirano, K. Okada, J. Hirokawa, and M. Ando, in Numerical Simulation–From Theory to Industry, edited by M. Andriychuk (InTech, 2012), Chap. 11, pp. 233–258 [http://www.intechopen.com/books/numerical-simulation-from-theory-to-industry].

[13] A. M. Mangan and S. P. Voinigescu, IEEE Trans. Electron Devices **53**, 235 (2006).

[14] E. K. Miller, *Time-Domain Measurements in Electromagnetics* (Springer, New York, 1986).

[15] J. R. Andrews, Picosecond Pulse Labs Application Note No. AN-15, 2004).

[16] Agilent Technologies, Inc Application Note No. 1287-02, 2012.